Optimization Of VAWT Via Coupled Guide Structure And Blade Pitch Angle

Xiaoju Yin[1*], Wei Zhang[1], Jian Wang[2], Yong Guo[3], Zijing Wang[1], and Tienan Yang[3]

[1] *School of New Energy, Shenyang Institute of Engineering,No. 18, Puchang Road, Shenbei New District, Shenyang, Liaoning 110136, P. R. China*
[2] *Shenyang Urban Investment New Energy Group Co., Ltd., Shenyang, Liaoning 110000, P. R. China*
[3] *Huaneng International Power Co., Ltd., Yingkou Power Plant, Yingkou, Liaoning 115007, P. R. China*
[*] *Corresponding author. E-mail: lnsolyxj@163.com*

Received: Jun. 06, 2026; Accepted: Jul. 24, 2026

The unsteady dynamic stall phenomenon in lift-type vertical axis wind turbines (VAWTs) severely limits their commercial deployment. This study proposes a strategy that integrates a circular-array air guide structure with blade pitch angle adjustment. The proposed "flow field enhancement–blade adaptation" coupling strategy employs the SST k-ω turbulence model to perform transient flow field analysis of a three-bladed VAWT under various operating conditions. Through numerical simulation, a combination of air guide structure and blade pitch angle $\beta = 10°$ was identified as the most effective configuration. The numerical results show that the synergistic combination of the air guide structure and a blade pitch angle of $\beta = 10°$ increases the peak power coefficient by 4.58% compared with the $\beta = 0°$ baseline, while the average torque is increased by 48.3% relative to a conventional VAWT without the guide structure. The results indicate that under the modified flow conditions produced by the guide structure, a positive pitch angle—which is typically suboptimal for an unguided VAWT becomes the most effective setting, highlighting the importance of treating the guide structure and blade pitch as a coupled system, offering a promising approach for urban VAWT applications.

Keywords: VAWT, dynamic stall, air guide structure, pitch angle, coupled configuration, numerical simulation.

http://dx.doi.org/10.6180/jase.202611_34.055

1. Introduction

Driven by global carbon neutrality targets[1], distributed wind energy has gained increasing attention as a complement to centralized wind power[2]. Recent studies have explored various guide vane and deflector configurations to enhance VAWT performance in distributed applications[3, 4]. Among VAWT designs, the Darrieus type is the most widely studied[5]. Its advantages-aerodynamic omnidirectionality, compact structure, low mounting height for the generator, and quiet operation[6]-make it a promising candidate for urban and distributed energy systems. However, Darrieus VAWTs suffer from low aerodynamic efficiency caused by dynamic stall[7, 8]and poor self-starting capability due to severe cyclic torque fluctuations during blade rotation[9], both of which hinder large-scale commercial deployment.

During rotation, the blade angle of attack of a VAWT varies periodically and dramatically. When it exceeds the static stall angle, the blade experiences a sharp drop in lift accompanied by a surge in drag. To address this, researchers have pursued two main approaches: blade aerodynamic control and flow field enhancement. Wang et al.[10]proposed adaptive deformable blades that adjust airfoil camber in response to surface pressure distribution, suppressing flow separation and raising the peak power coefficient by 14.56%. Cheng et al.[11] adopted a helical blade design to smooth torque fluctuations by distributing the blade phase angle along the span. Li et al.[12] developed a truncated-cone wind concentrator that improves starting torque by physically constraining and accelerating the inflow. Ghafoorian et al.[3] demonstrated that semi-directional airfoil guide vanes improve both the self-starting capability and overall performance of Darrieus VAWTs through optimized vane positioning. More recently, combined passive flow control and pitch angle strategies have emerged: Jiang et al.[13] achieved a 7.78% efficiency gain by pairing a dimple-Gurney flap with pitch angle adjustment, and Fatahian et al.[14] reported a 36% increase in Cp using leading-edge prism cylinders for passive flow control on Darrieus turbines.

Despite these advances, the coupled interaction between an external flow-guiding structure and blade pitch angle on Darrieus-type VAWTs has not been systematically investigated. Variable pitch strategies have shown over 200% Cp improvement in theoretical models[15], and geometric sensitivity analyses have identified key blade shape parameters governing stall suppression[16, 17], yet the coupling between external flow-guiding structures and blade pitch remains underexplored. This study addresses that gap by investigating the interaction between a circular-array air guide structure and blade pitch angle, and how this coupling reshapes the local velocity triangle at the blade[18]. As the incident wind passes through the guide structure, the flow is accelerated and redirected around the rotor, thereby shifting the blade pitch setting that maximizes power output. A pitch angle that is suboptimal for an unguided rotor may therefore become effective when coupled with the guide structure. This interdependence cannot be inferred from studying either factor in isolation. The work quantifies the aerodynamic response to different pitch angles under the modified flow field and identifies the most effective geometric-aerodynamic matching configuration for suppressing dynamic stall.

2. Methods

2.1. Wind turbine geometry

The three-bladed VAWT geometry is shown in Fig. 1. Three circular air-guiding structures, arranged uniformly around the rotor, guide and accelerate the incoming flow for smooth energy transfer. With the guide structure geometry held constant, the blade pitch angle is varied to assess its effect on aerodynamic performance. The blades employ a NACA 0018 symmetric airfoil, a profile widely used in Darrieus-type VAWTs for its favorable stall characteristics and structural simplicity. The main geometric parameters are listed in Fig. 1.

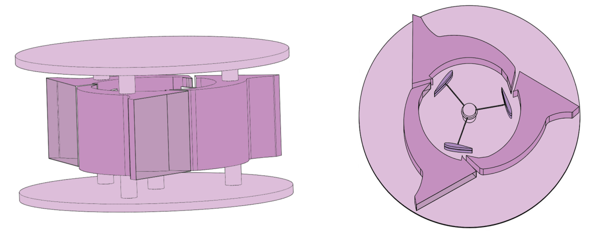

a.Side view of the wind turbine b.Top view of the wind turbine

Fig. 1. Geometric model of a vertical axis wind turbine with a circular array wind guide structure

2.2. Aerodynamic Loading Analysis

During rotation, a VAWT blade experiences higher lift than drag in the upwind region, yielding efficient energy extraction[7, 19]. In the downwind region, drag exceeds lift and energy capture is low[20]. To address this imbalance, a novel configuration was designed in which the air guide structure redirects and accelerates the incoming wind. As shown in Fig. 2, the circular-array guide structure ensures that the blades always operate in a favorable downwind environment. This reconfiguration alters the aerodynamic loading on the blade surfaces and significantly improves the energy extraction efficiency of the VAWT.

The relative velocity (W) of the jet velocity at the outlet of the air guide structure is superimposed with the rotational velocity. The velocity triangle shown in the red area in Fig. 2 is represented by the following vector relationship:

$$W = \sqrt{V_1^2 + U^2 + 2U_1 V \cos\theta} \quad (1)$$

Where V_1 is the outlet jet velocity, U is the blade tangential linear velocity, and W is the synthesized relative velocity.

$$\lambda = \frac{\omega R}{V_1} \quad (2)$$

Where ω is the rotor angular velocity(rad/s), R is the rotor radius (m).

2.3. Governing equations and turbulence models

The transient, three-dimensional, incompressible turbulent flow around the turbine was simulated. The flow field of a VAWT is characterized by strong unsteadiness, large-scale separation, and rotational curvature effects, making the unsteady Reynolds-averaged Navier-Stokes (URANS) equations an appropriate modeling framework[21]. Accurate estimation of the blade angle of attack is critical for VAWT simulations; geometrically derived AoA values can be unreliable under dynamic stall conditions. The local flow-field-based AoA estimation approach of Ouchene et

Table 1. Key geometric parameters of wind turbine and air guide structure

Feature	Quantity/Type
Number of blades	3
Type of blades	NACA0018
Blade chord length [C]	0.21m
Diameter [D]	1.4m
Height [H]	0.8m
Number of air guide structures	3
Wall thickness of guide structure	0.05m
Inner curvature radius of guide structure	0.81m
Outer curvature radius of guide structure	1.13m
Radial distance from rotor center to guide structure leading edge	1.24m
Import and export area ratio	3
Bending angle of air guide structure	120°

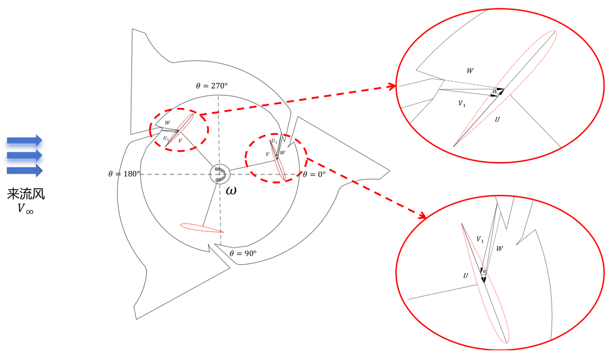

Fig. 2. Velocity triangle and aerodynamic analysis of the VAWT rotation cycle.

al. was therefore adopted[22]. The continuity and momentum equations for incompressible flow are:

$$\frac{\partial u_i}{\partial x_i} = 0 \tag{3}$$

$$\frac{\partial u_i}{\partial t} + u_j \frac{\partial u_i}{\partial x_j} = -\frac{1}{\rho}\frac{\partial p}{\partial x_i} + \frac{\partial}{\partial x_j}\left(v \frac{\partial u_i}{\partial x_j} - \overline{u_{i'} u_{j'}} \right) \tag{4}$$

In the above equations, u_i and x_i denote the velocity component and coordinate component in the i direction, respectively; t is time; p, ρ and v denote pressure, fluid density and kinematic viscosity, respectively. In formula (3), $-u_{i'} u_{j'}$ is the Reynolds stress tensor, which is used to characterize the effect of turbulent fluctuations on the mean flow. This term needs to be closed by introducing a turbulence model.

The SST $k - \omega$ turbulence model[23] was selected for this study. It solves transport equations for k and ω, blending the k - ω formulation near the wall with $k - \varepsilon$ behavior in the far field via a switching function F_1. The model is well-suited for adverse pressure gradients and flow separation-conditions typical of VAWT dynamic stall. Compared with the standard $k - \omega$ formulation, it is less sensitive to freestream turbulence; unlike the $k - \varepsilon$ model, it resolves the viscous sublayer directly without relying on wall functions.

The SIMPLE algorithm was used for pressure-velocity coupling. Pressure was discretized with a second-order scheme, and momentum was discretized with second-order upwind[24]. All simulations were performed using ANSYS Fluent 2024 R1.

2.4. Boundary Conditions

The computational domain and boundary conditions are shown in Fig. 3. To avoid inlet effects and allow full wake development, the domain extends 5D upstream and 20D downstream of the turbine, with a height and width of 10D[25]. The inlet velocity is set to 10 m/s; the rotational speed varies with tip speed ratio. The outlet is a pressure outlet at atmospheric pressure, with zero-gradient boundary conditions applied for k and ω. The top, side, and bottom boundaries are set as symmetry boundary conditions[25]. The rotating and stationary domains are connected through an interface, with a sliding mesh technique employed at the interface to handle the relative motion between the rotating and stationary domains [26]. The inlet turbulence intensity was set to 5% with a turbulence length scale of 0.1 m, corresponding to $k = 0.375\ m^2/s^2$ and $\omega \approx 11.18\ s^{-1}$. Near-wall mesh resolution was controlled to maintain $y^+ \approx 1$ on all blade surfaces, ensuring adequate resolution of the viscous sublayer for the SST $k - \omega$ model. The mesh meets standard orthogonality requirements, as shown in Fig. 3.

2.5. Validation of the numerical methodology

Mesh independence was analyzed at TSR = 2, as shown in Fig. 4 (a). To balance computational accuracy and resource consumption, tests were conducted on four different grid

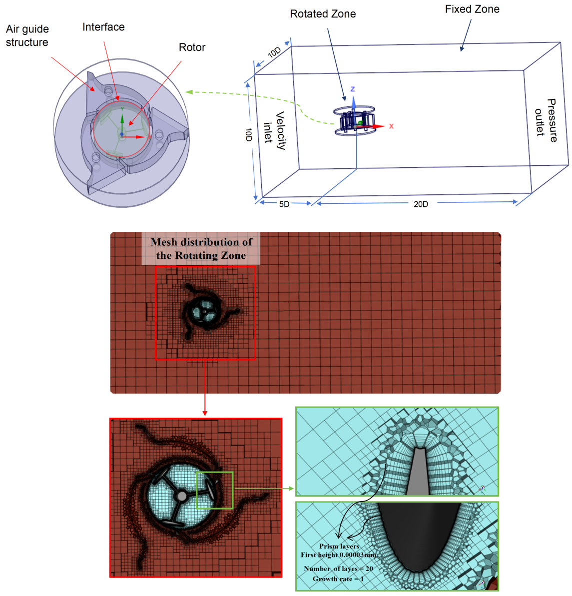

Fig. 3. Computational domain and mesh generation.

densities[27]. The average torque coefficient per revolution of the wind turbine was used as the monitoring index. The results show that when the number of meshs exceeds 16 million, the rate of change is less than 2%; when it reaches 20 million, the results tend to stabilize. Therefore, the 20 million grid scheme was ultimately selected for subsequent calculations.

The time step corresponded to 2° of rotor rotation per step. At each time step, scaled residuals were reduced to below 10^{-6} for continuity and 10^{-5} for momentum and turbulence equations. Data were sampled over the final three revolutions after the torque coefficient had reached a statistically steady periodic state, and the cycle-averaged power coefficient was obtained as the arithmetic mean of the instantaneous values over these revolutions.

To assess the reliability of the numerical approach, the present CFD methodology was applied to the wind-tunnel VAWT tested by Yang et al.[19] (two-bladed, NACA0021, $\mathrm{D} = 2.0\ \mathrm{m}, \mathrm{U_o} = 8.0\,\mathrm{m/s}, \beta = 6°$). The computed and measured single-blade torque coefficients are compared in Fig. 4 (b). The present CFD results capture the overall Torque coefficient variation with azimuth angle, including the primary peak near $\theta = 120°$, the secondary peak near $\theta = 240°$, and the low-torque regions at the upwind-downwind transitions. The present CFD results are in close agreement with the experimental measurements over the majority of the rotation cycle. The CFD curve lies modestly above the experimental data near $\theta = 45°$ and $\theta = 180°$, reflecting a slight overprediction of blade loading at these azimuth intervals. The overall consistency between the present CFD predictions and the experimental measurements supports the use of this numerical methodology for the VAWT configurations examined in this study.

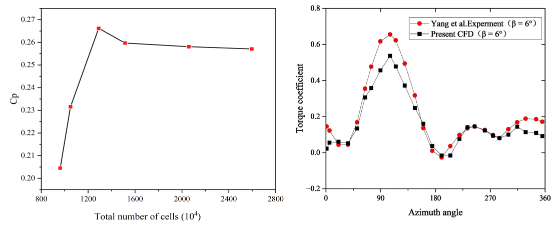

(a) Mesh independence verification of Cp with grid cell count

(b) Validation against wind-tunnel data of Yang et al. [19] (β = 6°)

Fig. 4. Validation of the numerical methodology.

3. Results and discussion

3.1. Analysis of the aerodynamic gain mechanism of the air guide structure

A comparative analysis was carried out between a conventional VAWT and the same turbine equipped with the proposed air guide structure. As shown in Fig. 5, the conventional VAWT (Fig. 5a) exhibits strong periodic fluctuations in blade lift coefficient with azimuth angle. Near $\theta = 90°$ in particular, the lift coefficient peaks sharply and then drop abruptly-a classic signature of dynamic stall. This behavior matches the dynamic stall patterns reported in recent Darrieus VAWT studies, where severe aerodynamic force oscillations accompany deep stall at high angles of attack[16, 17].

With the air guide structure in place (Fig. 5b), the lift peak broadens and flattens, and the high-frequency fluctuations are substantially reduced. This suggests the guide structure not only accelerates the flow but also conditions it: the walls suppress lateral fluctuations, lowering the turbulence level entering the rotor region and delaying boundary layer separation. The overall drag coefficient also drops markedly.

The lift-to-drag ratio comparison in (Fig. 5c) confirms that the air guide structure effectively blocks the reverse flow that would otherwise act on the returning blades, sharply reducing the reverse drag torque and improving overall aerodynamic efficiency. This mechanism resembles the effect of deflectors and guide vanes described in recent work, where redirecting flow away from the returning blade substantially cuts adverse torque[3, 28].

3.2. Coupling effect of pitch angle and airflow field

Because the air guide structure raises both the wind speed and alters the inflow angle, the pitch angle must be adjusted

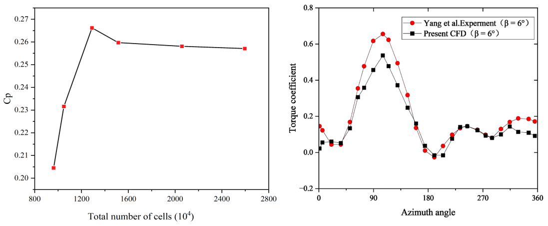

(a) Mesh independence verification of Cp with grid cell count

(b) Validation against wind-tunnel data of Yang et al. [19] (β = 6°)

Fig. 5. Aerodynamic coefficients and lift-to-drag ratio of the VAWT.

accordingly to achieve the best effect. Fig. 6 shows how different pitch angles influence the instantaneous torque at a fixed tip speed ratio, for both positive and negative pitch settings.

Positive pitch angle $(\beta > 0^{\circ})$: As shown in Fig. 6(a and b), at $\beta = 10^{\circ}$, the peak moment coefficient rises markedly and the azimuthal range of positive torque broadens. The accelerated flow through the guide structure increases the relative wind speed seen by the blades, which raises the effective angle of attack. A positive pitch angle geometrically reduces the angle of attack, exactly offsetting this increase and keeping the blades within the linear lift region, away from stall.

Negative pitch angle $(\beta < 0^{\circ})$: As shown in Fig. 6(c and d), negative pitch degrades performance. At $\beta = -10^{\circ}$ the torque drops sharply across most azimuth angles. Negative pitch further increases the already large effective angle of attack, driving the blade into deep stall as soon as it enters the windward zone and generating considerable pressure drag.

3.3. Response analysis of Cp with azimuth angle under different TSR for positive and negative pitch angles

To evaluate the robustness of the coupled optimization across operating conditions, Fig. 7 presents the three-dimensional response surface of Cp as a function of TSR and azimuth angle. The surface color and height represent the magnitude of Cp, giving a direct view of the turbine's energy capture topology.

At positive pitch angles ($\beta = 5^{\circ}$ and 10°, Fig. 7 a, b), the response surface exhibits a broad, ridge-like high-efficiency region. The high-power zone is distributed evenly across the rotation cycle. The positive pitch angle suppresses the deep-stall power drop common in conventional VAWTs, yielding smoother torque output.

By contrast, the negative pitch angles ($\beta = -5^{\circ}$ and -10°, Fig. 7 c, d) show sharp performance degradation. The high-efficiency region collapses into a narrow, island-like peak. Physically, the negative angle-of-attack offset triggers severe flow separation at high speed, causing the turbine to lose most of its power-generating capacity in the upper TSR range.

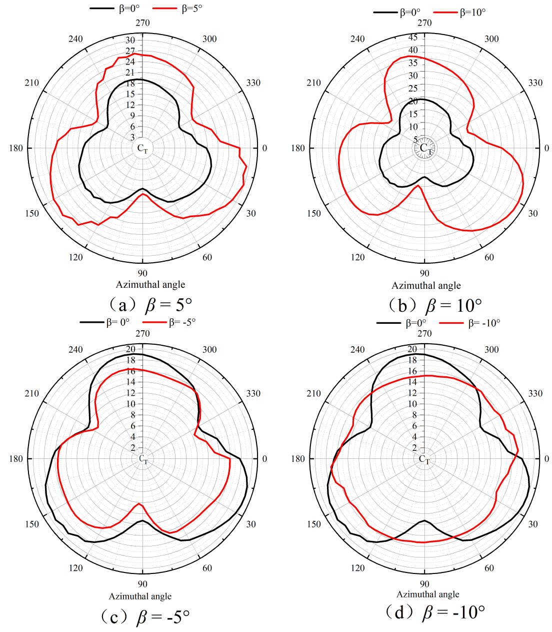

Fig. 6. Polar distribution of torque at different pitch angles.

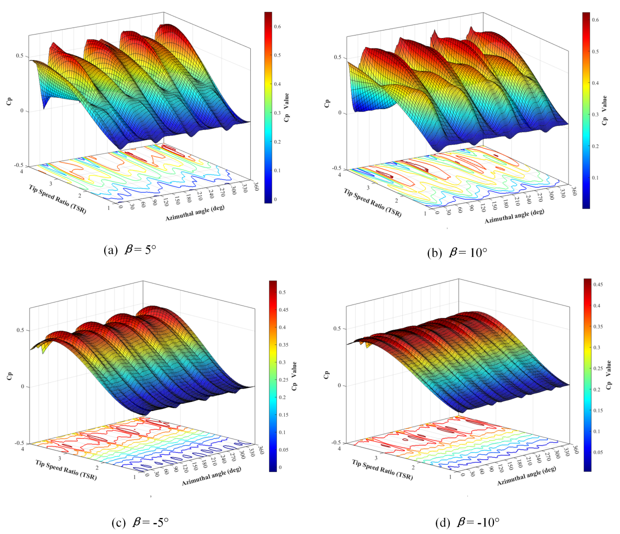

Fig. 7. Cp response surface vs. TSR and azimuth angle at different pitch angles.

3.4. Cp-TSR Characteristic Analysis

Fig. 8 compares the Cp-TSR curves to quantify overall energy capture. Condition $\beta = 10^{\circ}$ exhibits the best performance efficiency across the entire operating range, with a maximum Cp ≈ 0.44 at $\lambda \approx 3$, a significant improvement compared to the baseline original turbine (red dashed line, Cp ≈ 0.35). Notably, condition $\beta = 10°$ maintains high efficiency across a wide range of tip speed ratios, indicating better adaptability to variable speed wind conditions. While $\beta = 0°$ configuration shows improvement in the low TSR region, its performance drops substantially below that of $\beta = 5°$ in the high TSR region.

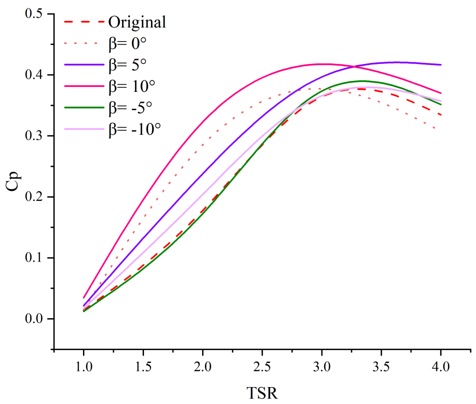

Fig. 8. Cp-TSR analysis of different models

3.5. Flow field analysis

The aerodynamic enhancement mechanism under the combined effect of the air guide structures and the blade pitch angles is analyzed. The velocity field distribution in the Z direction of different pitch angle models at different azimuth angles intuitively reflects the boundary layer evolution characteristics of the fluid around the blade, as shown in Fig. 9.

The mechanism by which the forward pitch angle suppresses flow separation is that, at the critical azimuth angle in the windward region, the blade is at its maximum angle of attack and is most prone to dynamic stall. For a single blade in the baseline condition ($\beta = 0°$), fluid adhesion is only significant at specific angles, indicating that boundary layer separation begins.

However, the suction surface has weak fluid adhesion at most angles, which is the main reason for the decrease in lift. At $\beta = 5°$, the adhesion of high-momentum fluid to the blade surface is significantly enhanced compared with the baseline. The forward pitch angle compensates for the increased effective angle of attack induced by the accelerated flow through the guide structure, keeping the blade within the attached-flow regime and delaying boundary layer separation. The blade wake under the forward pitch angle condition is noticeably wider than that at $\beta = 0°$, further confirming that flow separation is effectively suppressed.

In contrast, a negative pitch angle severely degrades the flow field. Observing the contour plot at $\beta = -10°$, in the region from 180° to 360°, the blade suction surface is completely covered by the low-speed vortex regions, which reduces the blade adhesion and causes the leading-edge vortex to detach prematurely. This not only increases pressure drag but also leads to severe turbulence in the downstream flow field, which is consistent with the sharp torque drop observed at $\beta = -10°$ in Fig. 6.

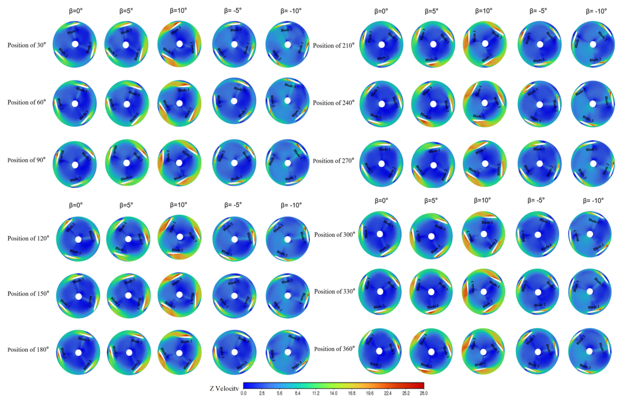

Fig. 9. Z-axis velocity contours at different azimuth angles and pitch angles.

4. Conclusion

Through numerical simulation, the synergistic influence of the air guide structure and blade pitch angle on the aerodynamic performance of a vertical axis wind turbine was systematically studied. The main conclusions are as follows:

1. The circular array of air guide structures utilizes the Venturi effect to increase the inflow velocity and simultaneously reshapes the flow field topology, improving the liftto-drag ratio by 0.307 compared with the conventional VAWT.

2. A positive pitch angle ($\beta > 0°$) geometrically compensates for the increased effective angle of attack produced by the accelerated flow through the guide structure. This prevents premature flow separation and suppresses dynamic stall. A negative pitch angle ($\beta < 0°$) has the opposite effect, intensifying separation and causing severe performance loss.

3. Through the synergistic effect of flow field enhancement and blade pitch adaptation, the average torque

is increased by 48.3% compared with the conventional VAWT without the guide structure. At a blade pitch angle of $\beta = 10^\circ$, the peak Cp is further improved by 4.58% compared with the $\beta = 0^\circ$ configuration. This 4.58% increment is achieved through pitch angle adjustment on top of the performance gain already provided by the guide structure. While modest in absolute terms, this result confirms that the most effective blade pitch angle under guided flow conditions differs from that of an unguided VAWT.

Acknowledgements

This work was supported by the Liaoning Provincial Education Science "14th Five-Year Plan" Project (Grant No. JG25DB334) and the Scientific Research Fund of Liaoning Provincial Education Department (Grant No. LJ212511632010).

References

[1] C. Sarmiento-Laurel, A. J. Díaz, I. Torres, R. Cáceres-González, and L. Silva-Llanca, (2025) *"3D numerical analysis of an H-rotor darrieus vertical axis wind turbine in transient regime"* **Energy *324***: 135849. DOI: 10.1016/j.energy.2025.135849.

[2] S. Roga, S. Bardhan, Y. Kumar, and S. K. Dubey, (2022) *"Recent technology and challenges of wind energy generation: A review"* **Sustainable Energy Technologies and Assessments *52***: 102239. DOI: 10.1016/j.seta.2022.102239.

[3] F. Ghafoorian, S. R. Mirmotahari, and H. Wan, (2024) *"Numerical study on aerodynamic performance improvement and efficiency enhancement of the savonius vertical axis wind turbine with semi-directional airfoil guide vane"* **Ocean Engineering *307***: 118186. DOI: 10.1016/j.oceaneng.2024.118186.

[4] A. Ulus and S. I. Moldovan, (2025) *"Optimization of Vertical Axis Wind Turbine Systems to Capture Vehicle-Induced Highway Winds"* **Energies *18***: 3139. DOI: 10.3390/en18123139.

[5] M. Khudri Johari, M. Azim A Jalil, and M. Faizal Mohd Shariff, (2018) *"Comparison of horizontal axis wind turbine (HAWT) and vertical axis wind turbine (VAWT)"* **International Journal of Engineering and Technology *7***: 74–80. DOI: 10.14419/ijet.v7i4.13.21333.

[6] A. Abdolahifar, H. Montazeri, and A. Zanj, (2026) *"Towards enhanced startup performance of Darrieus vertical-axis wind turbines: Key flow features at moderate tip speed ratios"* **Renewable Energy *256***: 123778. DOI: 10.1016/j.renene.2025.123778.

[7] M. Ahmadi-Baloutaki, R. Carriveau, and D. S.-K. Ting, (2016) *"A wind tunnel study on the aerodynamic interaction of vertical axis wind turbines in array configurations"* **Renewable Energy *96***: 904–913. DOI: 10.1016/j.renene.2016.05.060.

[8] J. Joseph, S. Sridhar, S. A., and J. Radhakrishnan, (2024) *"Analyzing dynamic stall on tubercle mounted VAWT blades: A simplistic experimental approach using an oscillating rig"* **Sustainable Energy Technologies and Assessments *71***: 103962. DOI: 10.1016/j.seta.2024.103962.

[9] O. Erkan, M. Özkan, Y. Çelik, and M. S. U. Khalid, (2025) *"Taguchi-based multi-factor analysis of self-starting behavior in vertical axis wind turbine farms"* **Energy *341***: 139495. DOI: 10.1016/j.energy.2025.139495.

[10] Y. Wang, X. Sun, X. Dong, B. Zhu, D. Huang, and Z. Zheng, (2016) *"Numerical investigation on aerodynamic performance of a novel vertical axis wind turbine with adaptive blades"* **Energy Conversion and Management *108***: 275–286. DOI: 10.1016/j.enconman.2015.11.003.

[11] Q. Cheng, X. Liu, H. S. Ji, K. C. Kim, and B. Yang, (2017) *"Aerodynamic Analysis of a Helical Vertical Axis Wind Turbine"* **Energies *10***: 575. DOI: 10.3390/en10040575.

[12] Y. Li, S. Zhao, K. Tagawa, and F. Feng, (2018) *"Starting performance effect of a truncated-cone-shaped wind gathering device on small-scale straight-bladed vertical axis wind turbine"* **Energy Conversion and Management *167***: 70–80. DOI: 10.1016/j.enconman.2018.04.062.

[13] T. Jiang, Q. Mo, and L. Luo, (2025) *"Study on the Effect of Pitch Angle on the Aerodynamic Characteristics of a Vertical Axis Wind Turbine with a Dimple-Gurney Flap"* **Journal of Physics: Conference Series *3086***: 012001. DOI: 10.1088/1742-6596/3086/1/012001.

[14] E. Fatahian, F. Ismail, M. H. H. Ishak, and W. S. Chang, (2024) *"Novel passive flow control method using leading-edge prism-shaped cylinder: Performance enhancement of vertical-axis wind turbines"* **Physics of Fluids *36***: 115170. DOI: 10.1063/5.0233464.

[15] A. Gupta, U. Ali, H. A. Abderrahmane, and I. Janajreh, (2025) *"Blade pitching in vertical axis wind turbines: A double multiple stream tube theoretical approach to performance enhancement"* **Heliyon *11***: e42101. DOI: 10.1016/j.heliyon.2025.e42101.

[16] A. Escudero Romero, A. P. Blasetti, J. G. Acosta-López, M.-Á. Gómez-García, and H. de Lasa, (2024) *"Vorticity and Its Relationship to Vortex Separation, Dynamic Stall, and Performance, in an H-Darrieus Vertical-Axis Wind Turbine Using CFD Simulations"* **Processes *12***: 1556. DOI: 10.3390/pr12081556.

[17] Q. Zhang, W. Miao, K. Zhao, C. Li, L. Chang, M. Yue, and Z. Xu, (2025) *"Influence of Geometric Effects on Dynamic Stall in Darrieus-Type Vertical-Axis Wind Turbines for Offshore Renewable Applications"* **Journal of Marine Science and Engineering *13***: 1327. DOI: 10.3390/jmse13071327.

[18] G. Tong, Y. Li, K. Tagawa, and F. Feng, (2023) *"Effects of blade airfoil chord length and rotor diameter on aerodynamic performance of straight-bladed vertical axis wind turbines by numerical simulation"* **Energy *265***: 126325. DOI: 10.1016/j.energy.2022.126325.

[19] Y. Yang, Z. Guo, Q. Song, Y. Zhang, and Q. Li, (2018) *"Effect of Blade Pitch Angle on the Aerodynamic Characteristics of a Straight-bladed Vertical Axis Wind Turbine Based on Experiments and Simulations"* **Energies *11***: 1514. DOI: 10.3390/en11061514.

[20] M. Islam, D. Ting, and A. Fartaj, (2008) *"Aerodynamic models for Darrieus-type straight-bladed vertical axis wind turbines"* **Renewable and Sustainable Energy Reviews *12***: 1087–1109. DOI: 10.1016/j.rser.2006.10.023.

[21] M. H. Shojaeefard, M. Tahani, M. B. Ehghaghi, H. Fallah Ardeshir, and M. Beglari, (2012) *"Corrigendum to Numerical study of the effects of some geometric characteristics of a centrifugal pump impeller that pumps a viscous fluid [Computers and Fluids 60 (2012) 61-70]"* **Computers and Fluids *64***: 157. DOI: 10.1016/j.compfluid.2012.06.014.

[22] S. Ouchene, A. Smaili, and H. Fellouah, (2024) *"On the estimation of the angle of attack for vertical axis wind turbines"* **International Journal of Numerical Methods for Heat and Fluid Flow *34***: 2626–2653. DOI: 10.1108/hff-09-2022-0566.

[23] F. R. Menter, (1994) *"Two-equation eddy-viscosity turbulence models for engineering applications"* **AIAA Journal *32***: 1598–1605. DOI: 10.2514/3.12149.

[24] W.-H. Chen, C.-Y. Chen, C.-Y. Huang, and C.-J. Hwang, (2017) *"Power output analysis and optimization of two straight-bladed vertical-axis wind turbines"* **Applied Energy *185***: 223–232. DOI: 10.1016/j.apenergy.2016.10.076.

[25] A. S. Saad, I. I. El-Sharkawy, S. Ookawara, and M. Ahmed, (2020) *"Performance enhancement of twisted-bladed Savonius vertical axis wind turbines"* **Energy Conversion and Management *209***: 112673. DOI: 10.1016/j.enconman.2020.112673.

[26] N. Kalassov, Z. Baizhuma, R. Manatbayev, A. Yershina, M. Isataev, A. Kalassova, Z. Seidulla, B. Bektibay, and B. Amir, (2025) *"Integrated Approach to Aerodynamic Optimization of Darrieus Wind Turbine Based on the Taguchi Method and Computational Fluid Dynamics (CFD)"* **Applied Sciences *15***: 5739. DOI: 10.3390/app15105739.

[27] M. Elkhoury, T. Kiwata, K. Nagao, T. Kono, and F. ElHajj, (2018) *"Wind tunnel experiments and Delayed Detached Eddy Simulation of a three-bladed micro vertical axis wind turbine"* **Renewable Energy *129***: 63–74. DOI: 10.1016/j.renene.2018.05.096.

[28] A. L. G. Santos, J. C. Martins, L. A. Isoldi, G. d. C. Dias, L. A. O. Rocha, J. A. Souza, and E. D. dos Santos, (2024) *"Numerical Analysis of the Influence of Rectangular Deflectors and Geometry of L-Shaped Channel over the Performance of a Savonius Turbine"* **Journal of Marine Science and Engineering *13***: 28. DOI: 10.3390/jmse13010028.